# A new method for the inversion of interferometry data using base functions derived from singular value decomposition of local measurements in tokamak plasmas

Ivo Furno†, Christopher Carey† and Henri Weisen‡‡

† *Los Alamos National Laboratory, M.S. E526, Los Alamos, NM 87545, USA and*
‡ *Centre de Recherches en Physique des Plasmas,*
*Association Euratom-Confédération Suisse, EPFL, Lausanne, Switzerland*

A novel method for inverting time-resolved line integrated interferometric plasma density measurements is described. The method uses singular value decomposition of local density profiles from Thomson scattering measurements obtained at low sampling rates in the same or equivalent plasmas to determine a set of orthogonal spatial basis functions which is well adapted to the physical processes under investigation. The sought-for density profile is expanded into a limited series of these functions and a solution is calculated by using a simple least-square fit method. The new method is compared to the Minimum Fisher Information (MFI) inversion method using artificial time-varying density profiles and is shown to be more accurate than MFI for reconstructing hollow electron density profiles. The small number of computations required provides for a fast algorithm. This method, which combines the high bandwidth of interferometer systems with the spatial accuracy of Thomson scattering, is applied to invert interferometer measurements in the Tokamak à Configuration Variable during normal and inverted sawtooth activity.

## I. INTRODUCTION

Understanding and control of particle transport is an important issue for thermonuclear fusion research since it determines the transport of the reactants and reaction products towards and away from the core of the plasma. Particle transport studies in plasmas require measurements of density profiles with high temporal and spatial resolution. In fusion research devices, two different diagnostics are commonly used to perform these measurements. Interferometer systems provide line integrated density measurements with high temporal resolution from the phase shift of a laser beam across the plasma cross section. Thomson scattering systems provide local density measurements by detecting the scattered laser light from a small volume of plasma. Although Thomson scattering systems have the advantage of providing local density profiles, their time resolution is limited by the repetition rate of the laser system and is usually inadequate for resolving fast transport phenomena. In contrast, interferometer systems have high sampling rates allowing fast changes of the line integrated density to be measured. However, because they are line-integrated they require solving an inverse problem for calculating the local density profile. Due to access limitations in tokamak devices, interferometer systems with a single fan of probing beams are the practical choice[1–3]. In this case, additional information about the structure of the electron density is required to solve the inverse problem. One possibility is to require the solution to satisfy some constraints. In the maximum entropy approach[4], the configurational entropy of the solution is minimized. The Minimum Fisher Information (MFI) method is par-

ticularly successful in inverting line-integrated interferometric data[2] by minimizing the Fisher Information[5] of the sought-for electron density distribution. The second possibility is to reduce the degrees of freedom of the problem by expanding the solution in series of orthogonal basis functions. In this approach, different functional forms have been used for interferometer data, i.e. Fourier-Bessel functions[6] or Gaussian functions[7]. However, these basis functions give good results only for specific data sets. No general and physically justifiable functional form exists for fitting electron density profiles in tokamak plasmas.

In this article, we develop a novel approach to inverting line integrated interferometer data by expanding the sought-for solution into a linear combination of basis functions that are well adapted to the physics determining the transport. The singular value decomposition (SVD) of the Thomson scattering measurements is used to determine these basis functions. In the following, we shall refer to the novel method, which combines the advantages of interferometry with those of Thomson scattering, as the Singular Value Decomposition Inversion (SVD-I) method.

The remainder of the article is organized as follows. In Sec. II, the far infrared interferometer and the Thomson scattering system on the TCV tokamak are described. In Sec. III, MFI and the expansion in basis function methods to perform interferometric inversion are presented. In Sec. IV, the SVD-I method is developed and compared to the MFI method using artificial data. Applications to experimental interferometer data in sawtoothing discharges in the Tokamak à Configuration Variable (TCV) are discussed in Sec. V. Finally, the conclusions are summarized in Sec. VI.
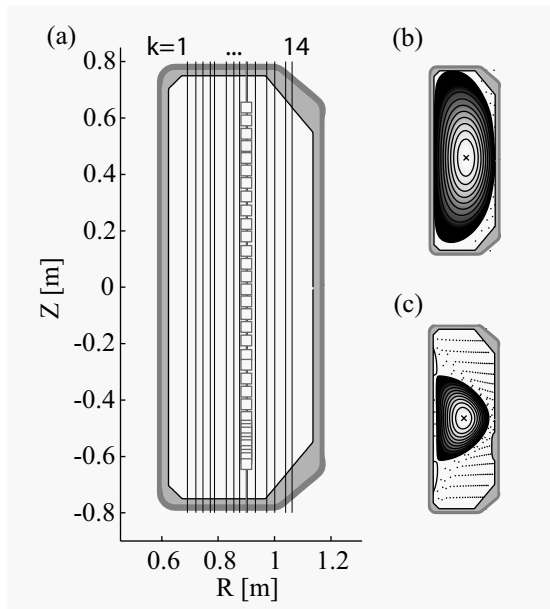
FIG. 1: Far Infrared Interferometer on TCV. (a) Geometrical arrangement of the 14 laser beams probing the plasma. Shown as squares are also the 25 scattering volumes of the TCV Thomson system. (b,c) Two extreme plasma shapes in TCV
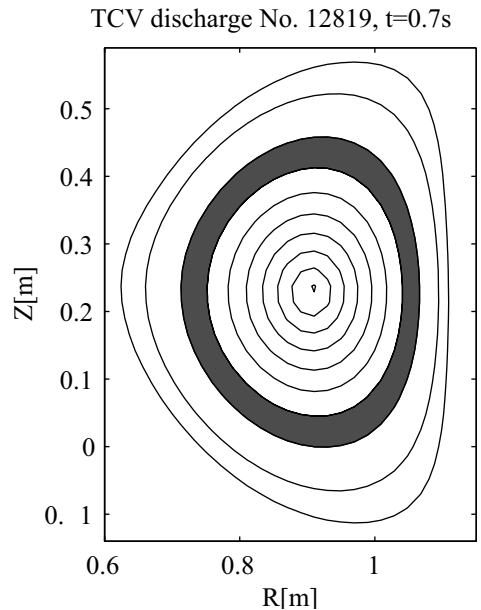


FIG. 2: Nested pixels corresponding to TCV magnetic flux surfaces as calculated by the equilibrium code LIUQE. Shown are magnetic flux surfaces corresponding to $\rho = 0.1 \cdot n$ for $n = 1, ..., 10$. The electron density is assumed constant in each pixel.

## II. EXPERIMENTAL SETUP

The TCV device[8] has a major radius $R_0 = 0.89$ m, minor radius $a = 0.25$ m and axial magnetic field $B_T \leq 1.54$ T. The TCV vacuum vessel allows for plasmas with elongations up to 2.9. Plasma shaping is performed with 16 independently controlled poloidal field coils. The radiofrequency system provides 3 MW of EC power for heating and current drive at the second cyclotron harmonic resonance (82.7 GHz) using the extraordinary mode[9].

Examples of an extremely elongated and an extremely triangular plasma are shown respectively in Fig. 1(b) and (c). The geometry of the magnetic flux surfaces is provided by the equilibrium reconstruction code LIUQE[10]. For practical calculations a grid of 41 equispaced points in the coordinate $\rho$ is used, where we have defined

$$\rho = \sqrt{\frac{\Psi - \Psi_0}{\Psi_a - \Psi_0}} \qquad (1)$$

$\Psi_0$ is the poloidal flux at the magnetic axis and $\Psi_a$ is the poloidal flux at last closed flux surface. In Fig. 2, an example of magnetic equilibrium reconstruction is given for the TCV discharge No. 12819. In this figure, the flux surfaces are shown at $t = 0.7$ s and correspond to $\rho = 0.1 \cdot n$, for $n = 1, ..., 10$.

On TCV, the electron density $n_e$ is obtained by interferometric and Thomson scattering measurements. The far infrared interferometric (FIR) system[3] uses an optically pumped $CH_2F_2$ laser with a wavelength $\lambda = 214.6$

$\mu$m corresponding to the cutoff density $n_c \approx 2.4 \cdot 10^{22}$ m$^{-3}$. The plasma is probed along 14 vertical chords of diameter $\approx 20$ mm in a single poloidal plane as shown in Fig. 1(a). The phase shift $\Delta\phi_i$ between a laser beam passing through the plasma along a straight optical path $L_i$ and a reference beam outside the plasma is measured by a Mach-Zehnder interferometer using heterodyne detection. The signal detectors (InSb hot electron bolometers) provide a frequency response up 100 kHz. For all experiments in TCV, the condition $n_e \ll n_c$ holds and the phase shift $\Delta\phi_i$ is proportional to the line integrated electron density

$$\Delta\phi_i = 6.0474 \cdot 10^{-19} \int_{L_i} n_e dl_i, i = 1, ..., 14 \qquad (2)$$

where $n_e$ is expressed in m$^{-3}$. At the selected wavelength, only minor refraction effects are present, even at high line averaged densities, $\overline{n}_e \approx 2.2 \cdot 10^{20}$ m$^{-2}$, and the precision of the measurement is typically $\Delta\overline{n}_e \approx 5 \cdot 10^{17}$ m$^{-2}$.

The TCV Thomson scattering system[11] also provides measurements of electron density profiles. Three nearly co-linear laser beams (wavelength $\lambda = 1.064$ $\mu$m, repetition rate to 20 Hz.) are injected from the bottom of the TCV vessel at the radial position $R = 0.9$ m. The light scattered from 25 sampling volumes, shown in Fig. 1(a), is collected with a spatial resolution of 40 mm in the vertical direction and 3 mm in the radial and toroidal directions. Sampling intervals down to 0.4 ms can be
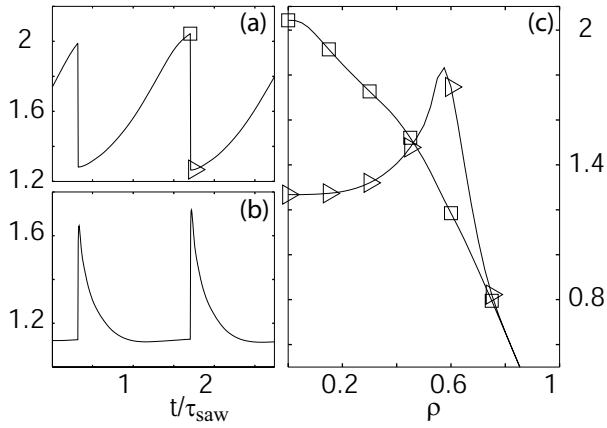
FIG. 3: Artificial local electron density measurements simulating sawtooth activity in the plasma. Time evolution of the electron density at different radial positions: (a) on axis; (b) just outside the inversion radius; (c) electron density profiles at different times indicated by different symbols in (a).
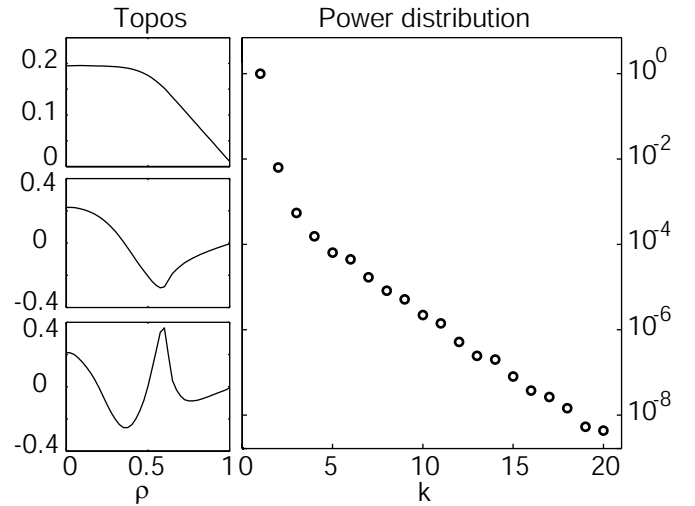


FIG. 4: Singular value decomposition of simulated Thomson scattering data. Thomson data are simulated by choosing a temporal subset of the artificial electron density data in Fig. 3. The first three topos are shown on the left together with the power distribution of the first twenty topo/chrono couples. 99.97% of the signal energy is stored in the first three topos.

achieved in the so-called 'burst-mode', when the three lasers are triggered close together.

## III. METHODS TO INVERT INTERFEROMETRIC DATA

From the mathematical point of view, the calculation of the local electron density profile $n_e$ from line integrated measurements requires the solution of the system of inhomogeneous *Fredholm* equations of the first kind in Eqs. 2. This system is always underdetermined, since an infinite number of measurements would be required to solve the system exactly.

On TCV, strongly shaped plasma configurations are produced so a simple Abel inversion[12] of this system of equations is not of much use. Under these circumstances, additional information is required to obtain a local electron density. Provided that the plasma is not perturbed by strong magnetohydrodynamic (MHD) activity, the electron density is expected to be constant on a toroidally symmetrical magnetic flux surface and depends on the radial flux coordinate $\rho$ alone, i.e. $n_e = n_e(\rho)$.

The supplementary information provided by the flux surfaces is introduced in the system of equations by defining nested pixels, $\rho_i \leq \rho \leq \rho_{i+1}$, determined by the geometry of the magnetic surfaces (shaded pixel in Fig. 2), within which the electron density is considered constant[2,13]. The electron density is discretized on this grid of nested pixels and the system of integral equations is thus transformed to a system of algebraic equations as

$$(\overline{n}_e)_i = \sum_{k=1,...,n_{pix}} T_{ik}(n_e)_i, i = 1,...,n_l \qquad (3)$$

which can be arranged in matrix form

$$\mathbf{\overline{n}_e} = \mathbf{T} \cdot \mathbf{n_e} \qquad (4)$$

The matrix element $T_{ik}$ equals the length of the optical path $L_i$ in pixel $k$. The line integrated measurements and the density profile form respectively column vectors $\mathbf{\overline{n}_e}$ of size $n_l$ (the number of line integrated measurements) and $\mathbf{n_e}$ of size $n_{pix}$ (the number of pixels). In practical situations, the number of line integrated measurements is limited by plasma accessibility resulting in the condition $n_l < n_{pix}$ and therefore the number of solutions is infinite.

One way to choose a physically sensible solution is to choose a density profile such that the functional

$$F = \chi^2 + \alpha R \qquad (5)$$

is minimized, where $\chi^2 = (\mathbf{T} \cdot \mathbf{n_e} - \mathbf{\overline{n}_e})^T \cdot (\mathbf{T} \cdot \mathbf{n_e} - \mathbf{\overline{n}_e})$ is the least-square term which provides the consistency of the solution with the line integrated measurements, $R$ is a regularization functional and $\alpha$ is a positive definite parameter. This parameter determines the weighting between the goodness of fit (represented by $\chi^2$) and the requirements imposed on the solution by the functional $R$.

One choice of $R$ that is particularly successful in inverting interferometric data is the Fisher-Information functional[2]

$$R_{FI} = \int \frac{[n_e'(\rho)]^2}{n_e(\rho)} d\rho \qquad (6)$$

where $n'_e(\rho)$ is the derivative of the electron density profile with respect to the radial flux coordinate $\rho$. In the frame of soft x-ray tomography[14,15], an efficient iterative scheme to minimize the functional $F_{FI} = \chi^2 + \alpha R_{FI}$ has been developed which utilizes the criterion $\chi^2 \approx n_l$ to determine the "correct" value of the parameter $\alpha$.

The second possibility to solve the system of Eqs. 3 is to reduce the degrees of freedom by expanding the local electron density profile into a series of orthogonal functions $w_k(\rho)$ such that

$$n_e(\rho) = \sum_{k=1,...,K_{max}} a_k \cdot w_k(\rho) \qquad (7)$$

which can be casted in the matrix form

$$\mathbf{n_e} = \mathbf{W} \cdot \mathbf{a} \qquad (8)$$

Using the expansion in Eq. 8, the set of Eq. 3 can be arranged in the matrix form

$$\mathbf{\overline{n}_e} = \mathbf{T} \cdot \mathbf{W} \cdot \mathbf{a} \qquad (9)$$

where the coefficients $\mathbf{a}$ are the unknowns of the system. The crucial issue in this approach is the choice of the base functions $w_k(\rho)$ in Eq. 7 which results in the condition $n_l \geq n_{pix}$. Provided that this condition is satisfied, the system of Eqs. 9 becomes an over-determined system for which a least squares solution can be determined by solving the set of normal equations[16]

$$(\mathbf{T} \cdot \mathbf{W})^T \cdot (\mathbf{T} \cdot \mathbf{W}) \cdot \mathbf{a} = (\mathbf{T} \cdot \mathbf{W})^T \cdot \mathbf{\overline{n}_e} \qquad (10)$$

In the next section, Thomson scattering measurements of electron density profiles are used to form the basis functions, $w_k(\rho)$, for the expansion of the local electron density profile as in Eq. 7.

## IV. NEW INVERSION METHOD USING SINGULAR VALUE DECOMPOSITION OF THOMSON SCATTERING DATA

In tokamak transport experiments, the temporal evolution of the electron density can be described by a time-dependent linear combination of spatial eigenfunctions of the operator that governs the dynamical response[17,19]. Using these particular eigenfunctions, a small number (typically from two to four) of components is usually required to model the evolution of the electron density profile[17] and therefore they constitute well-adapted base functions to reduce the dimensionality of the system of Eqs. 7. The SVD is particularly effective in identifying these basis functions from spatio-temporal data[18]. The SVD has also been successfully used in the analysis of soft x-ray[19,20] and magnetic[21] data and in image processing[22].

In this section, the SVD method and its fundamental properties are presented with particular application to Thomson scattering and interferometer data. Readers interested in a more rigorous mathematical derivation of the SVD can refer for example to Ref.[23]. The SVD-I technique is developed and an example using artificial electron density data is illustrated.

### A. Theoretical background on SVD

The SVD provides a decomposition of a $M \times N$ matrix $\mathbf{N_e}$ into three matrices $\mathbf{U}$, $\mathbf{S}$ and $\mathbf{V}$ such that

$$\mathbf{N_e} = \mathbf{U} \cdot \mathbf{S} \cdot \mathbf{V}^T \qquad (11)$$

The matrices $\mathbf{U}$ and $\mathbf{V}$ are $M \times M$ and $N \times N$ unitary matrices respectively, i.e. $\mathbf{U} \cdot \mathbf{U}^T = \mathbf{V} \cdot \mathbf{V}^T = \mathbf{I}$. The $M \times N$ matrix $\mathbf{S}$ is diagonal, i.e. $S_{km} = S_k \delta_{km}$, and the elements $S_{km}$ are either positive or equal to zero. Conventionally, they are ordered in descending order such that $S_1 \geq S_2 \geq \ldots \geq S_K$, where $K$ is equal to the rank of the data matrix $\mathbf{N_e}$.

This decomposition is the equivalent of the biorthogonal decomposition of the sampled signal[19] in which the data $n_e(\rho_j, t_j)$ are decomposed into a set of orthogonal spatial eigenmodes $u_k(\rho_j)$ composing the columns of $\mathbf{U}$, and orthogonal temporal eigenmodes $v_k(t_j)$ composing the columns of $\mathbf{V}$, such that

$$n_e(\rho_i, t_j) = \sum_{k=1,...,K} S_k u_k(\rho_i) v_k(t_j) \qquad (12)$$

where

$$\sum_{i=1}^{M} u_k(\rho_i) u_l(\rho_i) = \sum_{j=1}^{N} v_k(x_j) v_l(x_j) = \delta_{kl}. \qquad (13)$$

Following the nomenclature of Ref.[19], the spatial eigenmodes $u_k(\rho)$ will be called *topos* and the temporal eigenmodes $v_k(t)$ will be called *chronos*. The weights $S_k$ composing the diagonal of $\mathbf{S}$ will be referred to as *singular values*.

An important property of the SVD is its ability to concentrate most of the signal features from many dynamical systems in a limited and usually small number of biorthogonal components. For any $L \leq K$, the truncated expansion

$$y(x_i, t_j) = \sum_{k=1,...,L} S_k w_k(x_i) v_k(t_j) \qquad (14)$$

is the best approximation in the least-squares sense of the data among all possible sums of $L$ components. In practice, the singular values are strongly ordered and
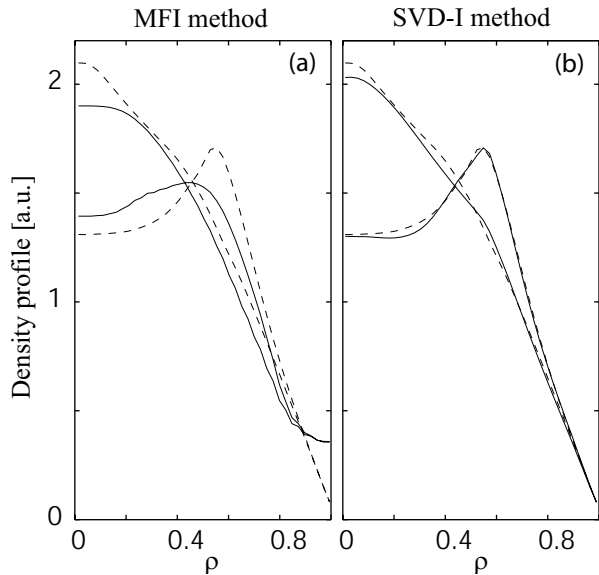
FIG. 5: Inverted electron density profiles (solid lines) from the simulated density profiles (dashed lines) shown in Fig. 3. The MFI and SVD methods are compared for peaked and hollow profiles.
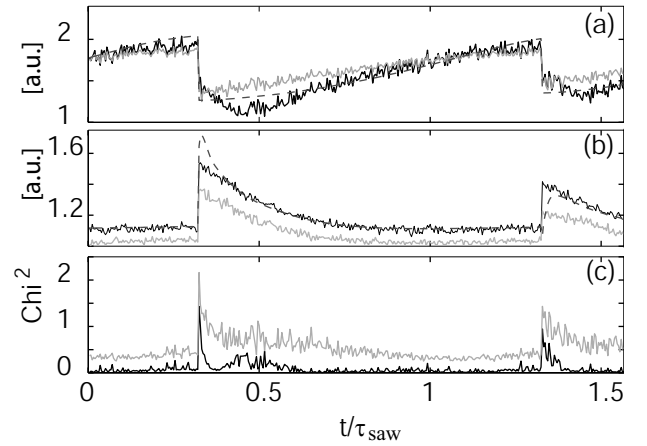


FIG. 6: Artificial electron densities. Time evolution of the electron density is shown as a dashed line, inversion of line integrated measurement by minimizing the Fisher information is shown as a light solid line, and inversion using the SVD is shown as a dark solid line for different radial positions: (a) on axis, and (b) just outside the inversion radius. Error of inversion methods in $\rho$ space is shown in (c) as a function of time.

the largest one exceeds the smallest one by a few orders of magnitude. The relative amount of energy, which is contained in each topo/chrono couple, is measured by the dimensionless energy

$$p_k = \frac{S_k{}^2}{E} \tag{15}$$

where the global signal energy is defined as

$$E = \sum_{k=1,\dots,K} (S_k)^2 \tag{16}$$

Another interesting property of the SVD method is the occurrence of two identical and non-negligible singular values in the presence of spatio-temporal symmetry of the signal[24]. In plasma physics applications, this is observed in the case of coherent phenomena such as rotating mode structures related to MHD instabilities[7,19,25].

### B. Development of the SVD-I method and comparison to MFI method

The basic idea of the SVD-I method to invert interferometric data is to expand the electron density profile in Eq. 7 by using basis functions $w_k(\rho)$ which are obtained from SVD analysis of Thomson scattering data. This choice of basis functions is well adapted to the physics determining the electron density profiles and therefore reduces the number of significant coefficients, $a_k$, in Eq. 9 allowing a least-square solution of the inverse problem as in Eq. 10. To illustrate the SVD-I method and

compare its performance to that of the MFI method, an artificial set of local density data, $\widehat{n}_e$, that simulates sawtooth activity has been generated (see Sec. V for details on sawtooth activity). The temporal evolution of the artificial electron density is shown in Fig. 3(a,b) for two different radial positions together with two profiles, Fig. 3(c), before and after the sawtooth crash. From these artificial data sets the line integrated density, $\overline{n}_e$, is calculated using Eq. 10. The transfer matrix $\mathbf{T}$ is obtained from an actual TCV discharge. Reconstructed local density profiles $n_e$ are obtained from both SVD-I and MFI method. The performance of the inversion techniques is thus revealed from a final comparison between $n_e$ and the initial $\widehat{n}_e$ input.

Thomson scattering measurements, which are used to form the base functions, are simulated in this example by choosing a temporal subset of $\widehat{n}_e$.

To apply the SVD, Thomson scattering electron density profiles $\widehat{n}_e(\rho_i, t_j)$ are arranged in matrix form as follows

$$\mathbf{N_e} = \begin{pmatrix} \widehat{n}_e(\rho_1, t_1) & \cdots & \widehat{n}_e(\rho_1, t_N) \\ \vdots & \cdots & \vdots \\ \widehat{n}_e(\rho_M, t_1) & \cdots & \widehat{n}_e(\rho_M, t_N) \end{pmatrix} \tag{17}$$

where $M$ and $N$ are respectively the number of spatial and temporal Thomson scattering samples. On TCV, the standard grid from the magnetic reconstruction code LIUQE assumes $M = 41$. By solving for the SVD of this matrix, as in Eq. 11, a set of orthogonal spatial eigenmodes, $u_k(\rho)$, is formed from the topos. Because these eigenmodes are determined from a direct local measurement of the electron density, they carry with them infor-
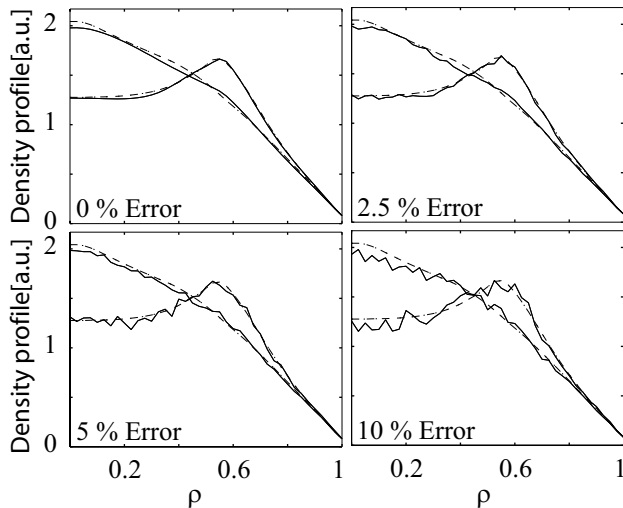
FIG. 7: Electron density profiles reconstructed using the SVD method from artificial line-integrated measurements. Different levels of noise are added on Thomson scattering profiles used to calculate the basis functions.
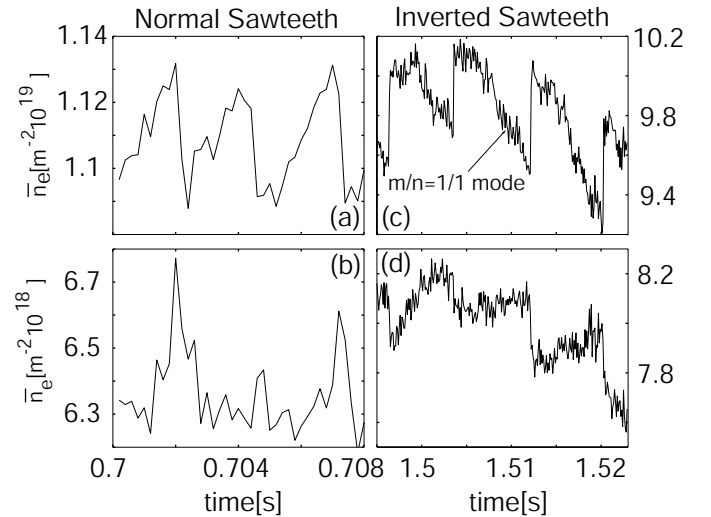


FIG. 8: Temporal evolution of line-integrated interferometric measurements during normal (a,b) and inverted (c,d) sawteeth. Shown are measurements along a central chord (a,c) and a chord just outside the sawtooth inversion radius (b,d).

mation about the spatial electron density distribution. In Fig. 4, the first three topos are shown together with the power distribution of the topos/chronos couples. As can be seen in this figure, the singular values are strongly ordered and 99.99% of the signal energy, as in Eq. 16, is contained in the first three chronos/topos pairs. Here, the local electron density is expanded as in Eq. 7 using the first three topos as the base functions, $w_k(\rho)$, and a simple least squares solution of Eq. 9 is found. A method to determine the number of components that are needed in the case of experimental data is presented in Sec. V.

In Figure 5, two artificial electron density profiles are shown (dashed lines), before and after the sawtooth crash, together with reconstructions from artificial line integrated data. Figure 5(a) shows MFI method, Fig. 5(b) the SVD-I method. For the same set of artificial data, the time evolution of the reconstructed electron density using both methods is shown for two different radial positions in Fig. 6(a,b). The time evolution of the artificial electron density is also shown as a dashed line for comparison. In Fig. 6(c), the time evolution of the error in the reconstruction defined as $\chi^2 = (\widehat{\mathbf{n}_e} - \mathbf{n_e})^T \cdot (\widehat{\mathbf{n}_e} - \mathbf{n_e})$ is shown.

In the case of the peaked profile, a good reconstruction is obtained with both methods for $\rho \leq 0.7$. However, the outermost region of the plasma, $\rho \geq 0.7$, is more accurately reconstructed by the SVD-I method. This is due to the sensitivity of the MFI functional in Eq. 6 to boundary conditions. In the case of the hollow electron density profile, inversions obtained using the SVD-I method are considerably more accurate than the MFI reconstructed profiles. The SVD-I method yields an accurate reconstruction through the entire plasma cross section, whereas the MFI method fails in reconstructing the strong density gradients in the region $0.4 \leq \rho \leq 0.7$. In

this region, the smoothing imposed on the solution by the Miminum-Fisher functional destroys features in the electron density profile, while the SVD-I profile maintains these features. This strength of the SVD-I method is obvious when we consider the time evolution of the $\chi^2$, as can be seen in Fig. 6(c).

TABLE I: The performance of the MFI and SVD algorithms. The CPU time on a PC workstation (Pentium 2, 600 MHz processor, 1 GB of RAM) under MATLAB 6.0 is shown for different numbers of time points.

| Method | 100pt | 300pt | 500pt |
|--------|-------|-------|-------|
| SVD    | 3.5 ms | 5.1 ms | 6.4 ms |
| MFI    | 15.9 s | 42.9 s | 73.9 s |

The performance of the SVD-I method has also been compared to that of the MFI method based on the runtime necessary for both inversions. One of the greatest strengths of the SVD-I method is the small number of computations required as compared to the MFI method resulting in faster inversion process. In Table I, a comparison of the time required to invert a set of artificial electron density profiles using both methods is shown. As the number of inversions is increased the time required for the MFI method increases almost linearly, while there is little change in the time required for the SVD-I method. It is worth noting that the number of inversions here is significantly less than the number of points sampled in a single TCV shot, which can have an average of 10,000 temporal samples in the interferometer measurement. Thus, the gain in computation time of the SVD-I method is tremendous when applied to actual data.
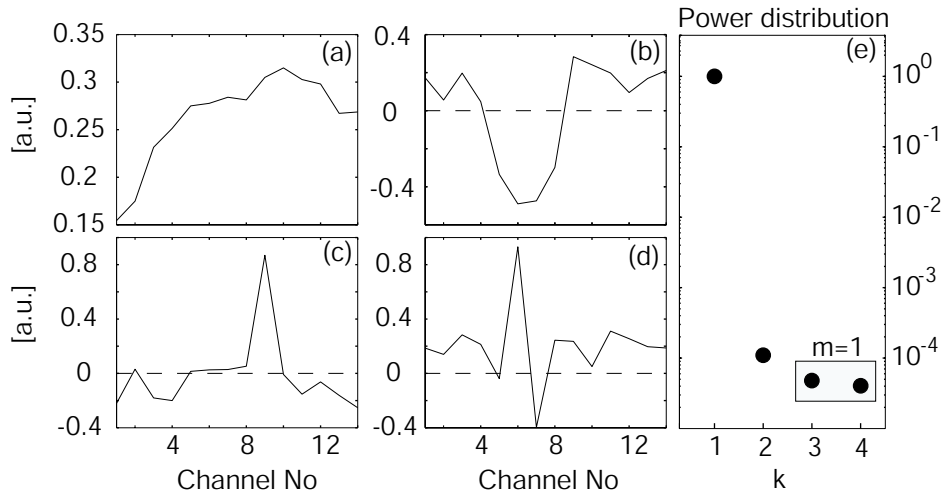
FIG. 9: SVD analysis of the 14 line integrated interferometric signals during inverted sawteeth in the time window shown in Fig.8. Shown are the topos corresponding to the four largest singular values (a-d) together with the distribution of the singular values (e). Two almost identical singular values, $k = 3, 4$, suggest the presence of a rotating mode.

### C.   The importance of errors in the Thomson data

For testing the effect of errors in the Thomson scattering measurements, reconstructions were produced from artificial line integrated data with three different levels of noise added on the simulated Thomson measurements: 2.5%, 5% and 10% respectively, the latter representing a rather pessimistic case compared to available experimental data. Figure 7 displays reconstructed peaked and hollow profiles for the different noise levels. As would be expected, as the level of noise in the Thomson measurements increases the level of noise in the reconstruction increases as well. However, even for the worst case scenario with 10% noise in the Thomson measurement, the reconstruction still conveys the major features of the electron density profile. We should also note here that the database of the local Thomson scattering profiles from which the base functions are derived, needs to be rich enough to contain sample profiles which are representative of all phases of the density profile evolution of interest. It is also important to note that base functions giving good reconstructions in a particular physical situation should not be expected to be suitable in different situations.

### V.   APPLICATION TO TCV INTERFEROMETRIC DATA

This section, which is not meant to be an extensive physics study, illustrates applications of the SVD-I method to experimental data during sawtooth activity in TCV plasmas.

Sawtooth oscillations, named after the characteristic shape of their soft x-ray time traces, were first observed on the ST tokamak[26] and are present in many tokamak experiments. In ohmically heated plasmas, they consist of periodic relaxations of the central electron temperature and density which develop when the safety factor on axis drops below unity. The sawtooth behavior for normal sawteeth is presented in Fig. 8(a,b) for TCV discharge No. 15279. The temporal evolution of the line integrated electron density, $\overline{n}_e$, is shown from a central interferometer chord, Fig. 8(a), and from a chord outside the inversion radius (see definition below), Fig. 8(b). Particle transport is ordinarily characterized by a negative (inward-directed) convective velocity that results in a slow rise (sawtooth ramp) of the line integrated central electron density $\overline{n}_{e0}$, Fig. 8(a), and moderately peaked electron density profiles. The sawtooth ramp phase is followed by a rapid drop (sawtooth crash) during which an $m/n = 1/1$ MHD instability grows (as indicated by soft x-ray tomographic reconstruction[25]) and particles are expelled from the central plasma region defined by $\rho \leq \rho_{inv}$, $\rho_{inv}$ being the inversion radius.

Although sawteeth have been observed and studied in all tokamaks, recent experiments have revealed new peculiar features when electron cyclotron heating (ECH) and electron cyclotron current drive (ECCD) are applied in sawtoothing tokamak discharges. In particular on TCV, with central ECH or ECCD, outward particle convection is observed when a quasi continuous $m/n = 1/1$ mode is present. This results in inverted sawteeth on the line integrated central electron density and hollow electron density profiles, whilst in the absence thereof, inward convection between successive sawtooth crashes leads to normal sawteeth[25,27]. The temporal evolution of line integrated interferometric data during inverted sawteeth is presented in Fig. 8(c,d) for TCV discharge No. 18549.

The application of the SVD-I method to real data requires the assessment of the number of components (NC) that are needed in Eq. 7 to expand the electron density
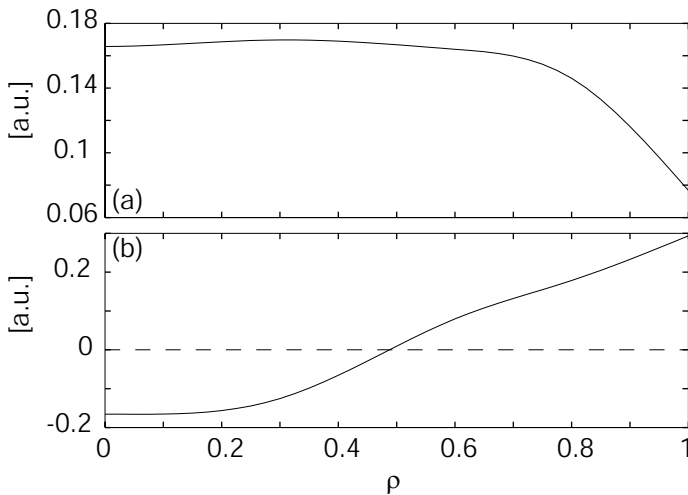
FIG. 10: SVD analysis od Thomson scattering measurements for TCV discharge No. 18549. Shown are the topos corresponding to the two largest singular values.
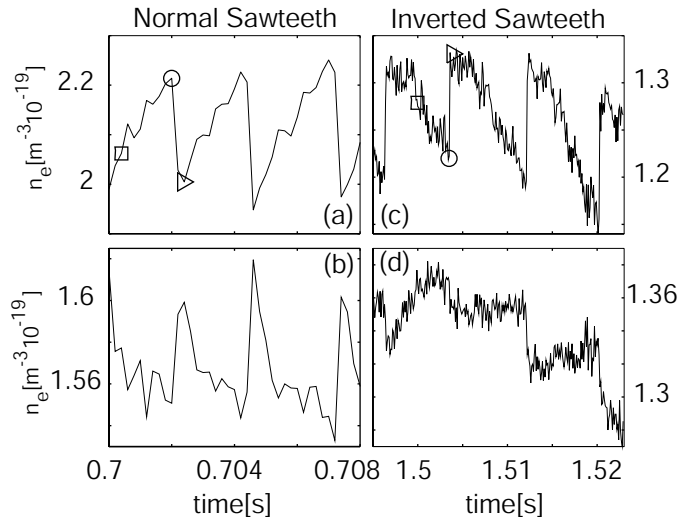


FIG. 11: Temporal evolution of local electron density reconstructed using the SVD method at different radial positions during both normal and inverted sawteeth for two TCV discharges shown in Fig. 8. (a,c) On-axis; (b,d) Just outside the sawtooth inversion radius.

profile and whether or not these components can be retrieved from SVD analysis of Thomson scattering data. Using TCV shot No. 18549 as an illustrative example, we discuss a method to determine the NC by comparing the SVD analysis of line integrated interferometric data to the SVD analysis of Thomson scattering data.

To apply the SVD, line integrated data from the 14 interferometer channels $\overline{n}_e(k, t_j)$ are arranged in matrix form as follows

$$\overline{\mathbf{n}_e} = \begin{pmatrix} \overline{n}_e(1, t_1) & \cdots & \overline{n}_e(14, t_N) \\ \vdots & \cdots & \vdots \\ \overline{n}_e(1, t_1) & \cdots & \overline{n}_e(14, t_N) \end{pmatrix} \quad (18)$$

where $N$ is the number of temporal samples and $k$ refers to the channel number as shown in Fig. 1.

In Fig. 9(a-d), the first four topos are shown from SVD analysis of the interferometric signals in the time interval of interest $t = 1.499 - 1.53$ s in Fig. 8. The power distribution of the singular values $S_k$, shown in Fig. 9(e), reveals four significant components that contain together more than 99.99% of the total signal energy. The first topo, Fig. 9(a), corresponding to the largest singular value, represents the contribution to the line integrated data of the spatially-averaged electron density profile. The periodic peaking-flattening of the profile during sawtooth activity is represented by the second topo in Fig. 9(b). Analysis of the singular value distribution shows two topos, corresponding to $k = 3, 4$ whose singular values are close enough to suggest the presence of rotating mode, Fig. 9(c,d). This is confirmed by the corresponding chronos (not shown here) which are oscillating at a frequency of $\approx 4$ kHz and phase shifted by $\pi/2$. This mode is localized at the positions of the interferometer channels $k = 6, 9$, which cross the plasma

at opposite sides of the magnetic axis, and therefore exhibits an $m = 1$ structure. This is also confirmed by soft x-ray data as detailed in Furno et al.[27]. Topos/chronos couples corresponding to higher singular values $S_k > 4$ are noise dominated and no coherent spatial and temporal structures are observed.

From this analysis, we can conclude that the SVD is efficient in separating the dynamics of the sawtooth activity (whose dominant structure is $m = 0$) from the rotation of the $m = 1$ mode. In particular in the present case, the sawtooth dynamics can be described by the truncated expansion

$$\overline{n}_e(k, t_j) = \sum_{l=1,2} S_l w_l(k) v_l(t_j) \quad (19)$$

where we have discarded topos/chronos couples that are not poloidally symmetric, i.e. corresponding to poloidal mode number $m \geq 1$. Since we have assumed a poloidally symmetric electron density distribution in the development of the SVD-I method, the presence of mode number $m \geq 1$ would result in errors in the reconstruction. Thus, the expansion in Eq. 19 provides the poloidally symmetric component of the density that can be inverted using the SVD-I method.

To assess whether or not the SVD of Thomson data can provide the correct base functions to expand the electron density, we apply the SVD to a set of Thomson scattering profiles measured during the same discharge as detailed in Sec. IV B. In Fig. 10, the first two topos obtained from SVD analysis of 60 Thomson scattering profiles for TCV discharge No. 18549 are shown. The first topo, corresponding to the largest singular value, represents
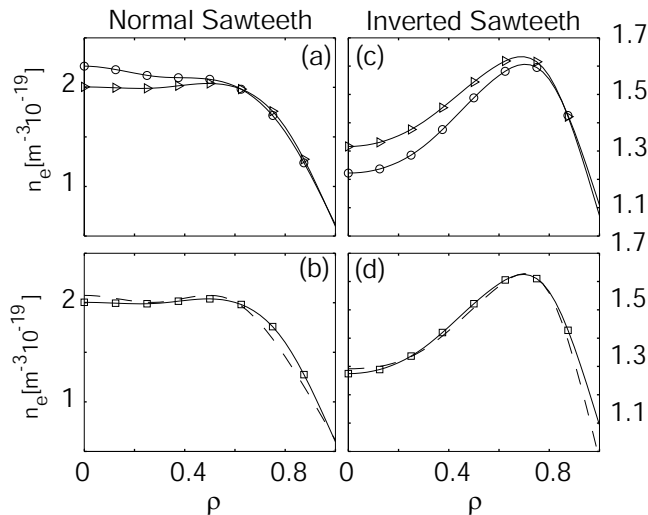
FIG. 12: Reconstructed electron density profiles using the SVD method during normal (left) and inverted (right) sawteeth. Times correspond to different symbols in Fig. 11. (a,c) Profiles before (circle symbols) and after (triangle symbols) the sawtooth crash. (b,d) Profile during the sawtooth ramp (square symbols) are compared with profiles as measured by the Thomson scattering system (dashed line).

the spatially-averaged electron density profile. The second topo represents the periodic flattening-peaking during sawtooth activity. We can therefore conclude that these two topos can be used to expand the electron density in Eq. 7 and a least-square solution can be found.

The same analysis has been performed for the normal sawtooth case of Fig. 8 resulting in the identification of two components describing the sawtooth dynamics. Also in this case, the topos corresponding to the first two largest singular values, as determined by SVD of Thomson scattering measurements, provide the correct basis functions to model sawtooth activity.

The temporal evolution of local electron density reconstructed using the SVD-I method is shown in Fig. 11 for both normal (a,b) and inverted sawteeth (c,d). For the same discharges, electron density profiles are shown in Fig. 12 at times indicated by different symbols in Fig. 11. In Fig. 12(b,d), inverted electron density profiles are compared with profiles as measured by the Thomson scattering system. In the normal sawtooth case, $n_{e0}$ increases during the sawtooth ramp and then drops at the sawtooth crash on a fast time scale (typically $\leq 100$ $\mu$s) resulting in a flattening of the electron density profile. After the sawtooth crash, the increase of $n_{e0}$ results

from a particle flux in the direction of the density gradient and hence from an inward particle convection, as shown by the temporal evolution of the electron density profile in Fig. 12(a,b). In the inverted sawtooth case, the decrease in $n_{e0}$ results from an outward particle flux which results in a hollowing of the density profile followed by a fast recovery at the sawtooth crash. In both cases, the SVD-I method yields a reconstruction of the electron density profile which is in excellent agreement ($\leq 5\%$) with the Thomson scattering profile as shown in Fig. 12(b,d). This shows that the SVD-I method can be successfully applied to experimental data.

## VI. SUMMARY

The SVD-I inversion method combines the high bandwidth of interferometer systems with the spatial accuracy of Thomson scattering. It uses SVD of temporally sparse local electron density profile measurements from a Thomson scattering system in the same or equivalent plasmas to determine a set of orthogonal basis functions which is well adapted to the physical processes under investigation. The sought-for density profile is expanded into series of a small number of these functions and a solution is calculated by using a simple least-square fit method. An SVD analysis of line integrated interferometer measurements allows the determination of the number of components that are needed to reproduce the evolution of the density profile in a particular situation. This information is used for optimizing the number of local base functions to include in the inversion. Using artificial data, we have shown that the SVD-I method is more efficient then the MFI method in reconstructing hollow density profiles and provides a faster algorithm for inverting the data. The SVD-I method has been applied to invert interferometric measurements from sawtoothing TCV plasmas. The reconstructed profiles are in excellent agreement with Thomson scattering measurements.

## VII. ACKNOWLEDGEMENTS

[1] K.L. Chiang *et al.*, Rev. Sci. Instrum. **68**, 894 (1997).

[2] J.P.T. Koponen and O. Dumbrajs, Rev. Sci. Instrum. **68**, 4038 (1997).

[3] S. Barry, Ph.D. thesis, National University of Ireland Cork, Published as Ecole Polytechnique Fédérale de Lausanne Report LRP638/99 (2001).

[4] B. Buck and V. A. Mackaulay, *Maximum Entropy in Action* (Oxford : Oxford University Press, 1991).

[5] B.R. Frieden, J. Mod. Opt. **35**, 1297 (1988).

[6] H. Ruan and B. Wan, International Journal of Infrared

and Millimiter Waves **21**, 1973 (2000).

[7] I. Furno, Ph.D. thesis No. 2434, Ecole Polytechnique Fédérale de Lausanne (2001).

[8] F. Hofmann *et al.*, Plasma Phys. Controlled Fusion **36**, B277 (1994).

[9] T. P. Goodman *et al.* , in *Proceedings of the 19th Symp. on Fusion Technology, Lisbon, (North-Holland, Amsterdam 1997)* (1996), vol. 1, p. 565.

[10] F. Hofmann and G. Tonetti, Nucl. Fusion **28**, 1871 (1988).

[11] R. Behn *et al.*, in *Proceedings of the 7th Int. Symp. Laser Aided Plasma Diagnostics, Montreux, 2002* (1995), vol. 26B, p. 392.

[12] I. Hutchinson, *Principles of plasma diagnostics* (IOP Publishing Ltd 2000, 1987).

[13] J. H. Williamson and D. E. Evans, IEEE Trans. Plasma Sci. **PS-10**, 82 (1982).

[14] M. Anton *et al.*, Plasma Phys. Controlled Fusion **38**, 1849 (1996).

[15] J. Mlynar *et al.*, Plasma Phys. Controlled Fusion **45**, 169 (2003).

[16] W. H. Press, *Numerical recipes in Fortran* (Cambridge University Press, 1992).

[17] J.M. Moret and Tore Supra Equipe, Nuclear Fusion **32**, 1241 (1992).

[18] G. H. Golub, *Matrix Computations* (Baltimore : Johns Hopkins University Press, 1996).

[19] T. Dudok de Wit *et al.*, Physics of plasmas **1**, 3288 (1994).

[20] C. Nardone, Plasma Phys. Controlled Fusion **34**, 1447 (1992).

[21] J. S. Kim *et al.*, Plasma Phys. Controlled Fusion **41**, 1399 (1999).

[22] T. S. Huang, Appl. Opt. **14**, 2213 (1975).

[23] J. Stoer and R. Bulirsh, *Introduction to numerical analysis* (Springer, New York, 1980).

[24] N. Aubry, Journal of Statistical Physics **81**, 793 (1995).

[25] I. Furno *et al.*, Nucl. Fusion **41**, 403 (2001).

[26] S. Von Goeler *et al.*, Phys. Rev. Letters **33**, 1201 (1974).

[27] I. Furno and H. Weisen, Phys. Plasmas **10**, 2422 (2003).